Performance-based design for earthquake-induced liquefaction: application to offshore energy structures

Haoyuan Liu[1][0000-0001-8728-332X] and Amir M. Kaynia[2,3][0000-0002-7774-3860]

[1] Norwegian Geotechnical Institute (NGI), Sognsveien 72, 0806 Oslo, Norway
[2] Norconsult AS, Vestfjordgaten 4, N-1338 Sandvika, Norway
[3] Norwegian University of Science and Technology (NTNU)
7491 Trondheim, Norway

amir.kaynia@ntnu.no

Abstract. Liquefaction has been a major challenge to design of structures founded on loose silt and sand in moderate and specially highly seismic regions. While assessment of liquefaction susceptibility and potential have been largely based on empirical methods, the design of structures on liquefiable soil requires reliable numerical tools and clear performance criteria. In this paper, solutions are provided based on the well-established SANISAND model and its more recent extension, SANISAND-MSu, implemented in the open-source finite element platform OpenSEEs. Applications are presented for structures commonly encountered in offshore energy sector such as conventional subsea facilities on mudmats and offshore wind turbines founded on large-diameter monopiles. The impact of pore-water pressure, and ultimately liquefaction, on the offshore structures is assessed by performing both quasi-static cyclic loading and earthquake shaking. The general behavior of these offshore structures during liquefaction are presented from a numerical modelling perspective. The simulation results indicate that the response of these structures is considerably affected by structural features and environmental loading conditions. The results presented in this work motivates the use of SANISAND-MSu model in enhanced 3D finite element modelling in offshore structural dynamic analyses.

Keywords: earthquake, pore-water pressure, numerical modelling, constitutive model, dynamic.

1 Introduction

The proportion of the renewable energy in the overall energy consumption has kept increasing in recent years. Offshore energy as an important component of the renewable energy is in tune with the trend and experiencing rapid growth in energy share. The global offshore wind capacity cumulated to about 22 GW in 2019 and is expected to reach about 100 GW in 2030 [1]. In the longer term, European Union aims to make offshore energy the main electricity source by 2040. Offshore wind will be a key element in the renewable energy considerations in the years to come [2].

The offshore energy-related structures have been constructed mostly in the areas with low seismicity. The research performed in the relevant subject span from experimental studies [3]-[8] to numerical investigation [9]-[12]. The growth of the construction of structures related to offshore energy in seismic regions requires a comprehensive understanding of the impact of liquefaction on these structures [13].

The main challenge is that the soil behaviour is in practice undrained or partially drained during load cycles in most dynamic excitations including earthquakes [14]. The accumulation of strain and pore-water pressure in the soil domain during the dynamic loading can change the soil's stiffness and strength significantly, which in turn alters the dynamic structural response [15]. Besides, during earthquake shaking, the combined effect from the environmental load may lead to a distinct behaviour of offshore structures.

Significant efforts have recently been devoted to the study of the dynamic response of offshore structures using three-dimensional Finite Element (3D FE) analysis enhanced by advanced implicit constitutive models (here 'implicit' is used to refer to models that calculate soil stress-strain response in incremental sub-septs). For instance, 3D FE analysis of monopile dynamic behaviour is investigated by Corciulo et al. [16] using multi-surface model [17], and by Kementzetzidis et al. [18] and Esfeh and Kaynia [14] using bounding surface SANISAND04 model (where SANISAND04 is used here refers to the original simple anisotropic sand model developed by Dafalias and Manzari in the 2004 [19]). Recently, Esfeh et al. [20] numerically studied the seismic response of subsea structures on caissons and mudmats with SANISAND04 as the constitutive model in FLAC3D.

Accurate implicit 3D FE analysis of structural dynamic response rely on the simulation ability of the adopted constitutive models. Proper capturing of soil cyclic behaviour at element level is required to evaluate the performance of constitutive models at both qualitative and quantitative levels. Recently, Liu et al. [21] adopted the concept of 'memory surface' [22] to realistically reflect sand fabric evolution (and effects) on sand cyclic behavior, based on Dafalias and Manzari's SANISAND04 model framework (denoted by SANISAND-MS). The model presents considerable improved accuracy compared with many other models when simulating drained ratcheting behaviour of sand. Later, Liu et al. [23] improved SANISAND-MS on aspects of hardening rule and flow rule for better simulation of undrained cyclic behaviour of sand. For this reason, the model is referred to as SANISAND-MSu in this work. SANISAND-MSu model can predict with good accuracy the cycle-by-cycle pore water pressure evolution and accumulation in the soil pre-dilative straining process. Besides, SANISAND-MSu predicts realistic strain accumulation in cyclic-mobility regime. The model has been successfully implemented in the open-source finite element platform OpenSEEs and shows good prediction abilities in simulating monopile response with the presence of pore-water pressure in quasi-static cyclic loading events [24].

Due to its promising performance at both element and finite element levels, SANISAND-MSu model is employed in this study to further investigate the dynamic response of different structures used in offshore energy. For completeness, a conceptual introduction to the SANISAND-MSu model is presented together with the model performance in reproducing element-level cyclic response. Then simulation results for

quasi-static cyclic response of a typical offshore monopile are presented using SANISAND-MSu model in 3D FE analysis with emphasis on the pore-water pressure effects. In the end, dynamic responses of two types of structures in offshore energy are studied. The selected structures include wind turbines on an extra-large 'XL' monopile and subsea manifolds on mudmat foundation. The focus of the dynamic analyses is: (1) the combined effect of earthquake shaking and wind load on XL monopile, and (2) the effect of mass distribution on the earthquake response of mudmat.

2 SANISAND-MSu model

SANISAND-MSu model was developed mainly for the simulation of undrained cyclic behaviour of sand with the objective of accurate simulation of pore pressure generation and cyclic mobility. Some key features of the SANISAND-MSu model are summarized in this section.

SANISAND-MSu model adopts bounding surface plasticity theory and is built based on the SANISAND04 model proposed by Dafalias and Manzari [18]. Sand fabric is taken into consideration in SANISAND-MSu model through the so-called 'memory-surface'. Fabric evolution takes place during both plastic contraction and dilation. Compared with SANISAND04, within which sand fabric only evolves and activates during the post-dilative stage, SANISAND-MSu simulates the effects of soil fabric in the whole plastic deformation stage. Such an improvement allows realistic simulation of sand cyclic behaviour under both drained and undrained conditions [21, 23]. The model follows critical soil state theory. Soil contractive/dilative behaviour is determined through the well-established 'state-parameter' concept [25]. Such features allow the model to simulate the behaviour of a given sand over wide density range with a single set of model parameters.

SANISAND-MSu model includes four loci. Fig. 1 illustrates the model loci in the deviatoric stress ratio plane:

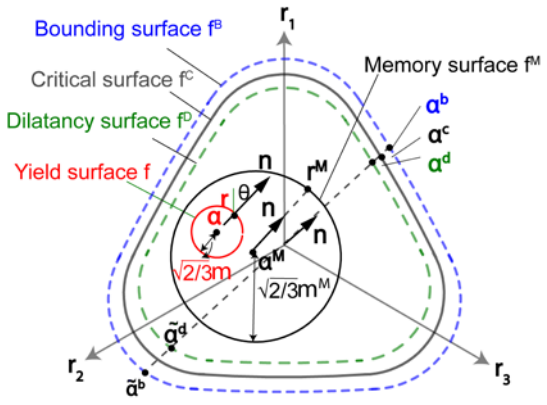

Fig. 1. SANISAND-MSu model loci in the deviatoric stress ratio plane.

1. A circular yield surface (f) that defines a pure elastic range;
2. An Argyris-shaped bounding surface (f^B) that encloses the admissible soil state. The bounding surface is associated with critical state through state parameter;
3. An Argyris-shaped dilatancy surface (f^D) that distinguishes contractive state from dilative soil state. The dilatancy surface is defined through state parameter;
4. A circular memory surface (f^M) that evolves during plastic deformation and is related to the evolution of stress-induced anisotropy.

The memory surface tracks the evolution of soil fabric during the plastic straining. SANISAND-MSu model [23] improves the original SANISAND-MS model [21] on two aspects, namely, proper simulation of sand fabric evolution history effects and stress-ratio effects.

The SANISAND-MSu model uses kinematic hardening rule and adopts non-associated flow rule. Soil stiffness is determined through distances between (a) yield surface and memory surface and (b) yield surface and bounding surface. Besides, the stress ratio effects are introduced in the hardening coefficient. Such modifications allow SANISAND-MSu to accurately predict the cycle-by-cycle pore-water pressure accumulation. Fabric evolution history and lode angle effects are introduced in the dilatancy coefficient to predict realistic strain accumulation in the cyclic mobility regime.

2.1 Stress-strain and pore pressure accumulation

The performance of SANISAND-MSu model is investigated here by comparing the results from the undrained cyclic triaxial tests [26] with model simulation results. The selected sand is Karlsruhe fine sand, with the following soil index properties: maximum void ratio $e_{max} = 1.054$, $e_{min} = 0.677$, soil uniformity coefficient $C_u = \frac{D_{60}}{D_{10}} = 1.5$ and medium particle diameter $D_{50} = 0.14$ mm. SANISAND-MSu parameters are calibrated against drained monotonic, undrained monotonic and undrained cyclic triaxial tests as summarized in [23]. The parameters are summarized in Table 1.

Table 1. SANISAND-MSu model parameters for Karlsruhe fine sand: calibration against triaxial test results from [26].

Elasticity		**Critical state**					**Plastic modulus**		
G_0	ν	M_c	c	λ_c	e_0	ξ	h_0	c_h	n^b
95	0.05	1.35	0.81	0.55	1.035	0.36	7.6	0.97	1.2
Yield	**Dilatancy**					**Memory surface**			
m	A_0	n^d	β_1	β_2	k	μ_0	ζ	w_1	w_2
0.01	0.74	1.79	4	3.2	2	65	0.0003	2.5	1.5

Fig. 2 compares the experimental results (Fig. 2a-b) with the simulation results from both SANISAND-MSu model (Fig. 2c-d) and SANISAND04 model (Fig. 2e-f). The test conditions are: relative density D_r=80%, initial confining pressure p=200 kPa, cyclic amplitude q^{ampl}=50 kPa.

In general, both SANISAND-MSu and SANISAND04 models capture the main features of the undrained cyclic triaxial behaviour of sand – i.e., reduction of mean effective stress p with loading cycles in the pre-dilative regime and cyclic mobility behaviour (repetitive increasing and decreasing mean effective stress butterfly loop with cycles). Note that SANISAND04 clearly overestimate the reduction of p for each loading cycle while SANISAND-MSu predicts more accurately the cycle-by-cycle pore-water pressure evolution. This is also demonstrated by Fig. 3 which shows the pore water pressure ratio r_u (defined as $1 - \sigma_v/\sigma_{v0}$, where σ_v is the vertical effective stress and σ_{v0} is the initial vertical effective stress prior to shearing) against number of loading cycles N. SANISAND-MSu model predicts 76 loading cycles to trigger the initial liquefaction (i.e., the first time p approaches 0), which agrees well with the experimental result (indicating 74 loading cycles to trigger initial liquefaction). However, SANISAND04 model suggests only 5 cycles to trigger initial liquefaction.

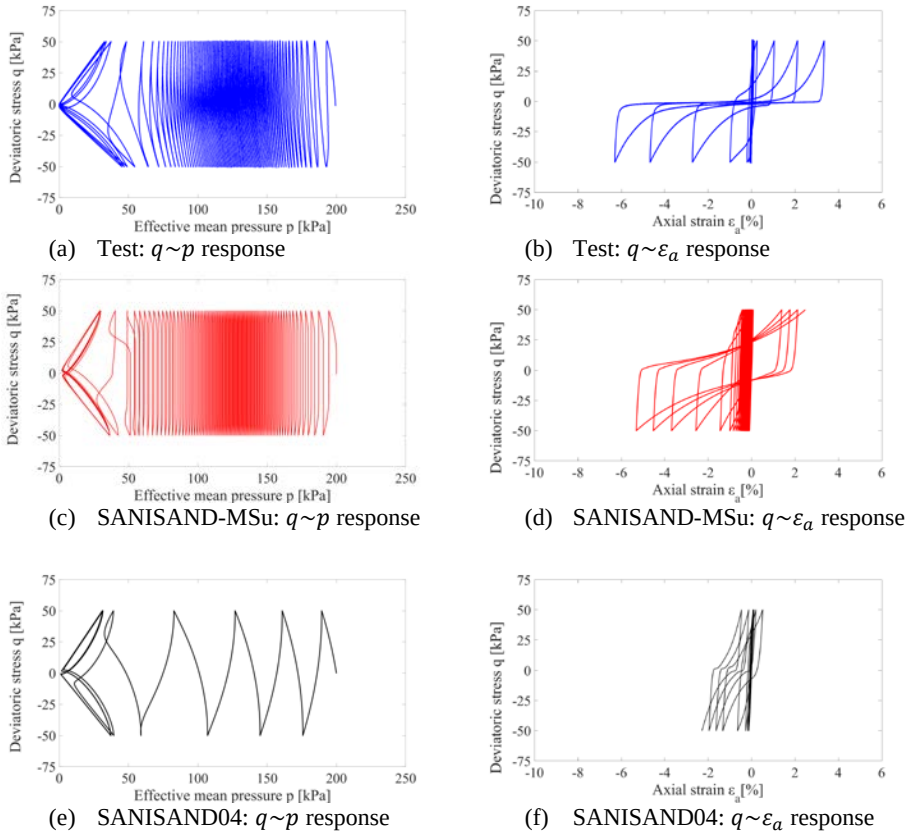

(a) Test: $q \sim p$ response (b) Test: $q \sim \varepsilon_a$ response

(c) SANISAND-MSu: $q \sim p$ response (d) SANISAND-MSu: $q \sim \varepsilon_a$ response

(e) SANISAND04: $q \sim p$ response (f) SANISAND04: $q \sim \varepsilon_a$ response

Fig. 2. Undrained cyclic triaxial tests: comparison among: (a)-(b) experimental result [26], (c)-(d) SANISAND-MSu simulation result and (e)-(f) SANISAND04 simulation result.

Another important improvement of SANISAND-MSu is that it can predict realistic strain accumulation in the cyclic mobility regime. As indicated in Fig. 2b, under stress-

controlled undrained triaxial condition, axial strain accumulate in both positive and negative directions. The phenomenon has been properly captured by SANISAND-MSu (Fig. 2d). However, SANISAND04 model suggests an accumulation of axial strain only in the negative direction (Fig. 2f).

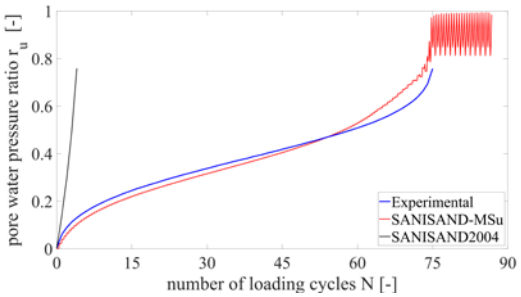

Fig. 3. Evolution of pore-water pressure ratio against number of cycles: comparison between experimental result [26], SANISAND-MS simulation and SANISAND04 simulation results.

2.2 Stiffness reduction and damping

While the ability for prediction of the pore-pressure generation is an important feature of a constitutive model, it is also important to have knowledge about the stiffness variation and hysteretic damping during cyclic loading. These two characteristics steer the dynamic response of the soil domain and soil-structure dynamics. A common method to assess these features is through the variation of the stiffness reduction $G/G_{max}$and damping with shear strain γ, as exemplified by Fig. 4a and Fig. 4b, respectively. The shear modulus G is the peak-trough soil secant shear modulus during a stress cycle and G_{max} is the initial shear modulus. Realistic reproduction of the variation of soil stiffness and damping is thus an important aspect to evaluate a constitutive model.

The performance of SANISAND-MSu in terms of shear modulus reduction (Fig. 4a) is investigated by comparing the model simulation results with two empirical results from the literature [27, 28] for different relative densities D_r in the range 40%~80%. The comparison suggests that while the trend is captured properly, SANISAND-MSu predicts greater shear stiffness for the same shear strain level.

The material damping ratio is defined as the ratio between the dissipated energy and the maximum potential energy during a load cycle. Fig. 4b shows the damping ratio predicted by SANISAND-MSu for the first stress cycle but sheared to different shear strain levels. Different relative densities $D_r = 40\%$, 60% and 80% are selected. The simulation results are compared with the empirical data by Darendeli [28] and Masing rule. Masing rule generally yields large damping ratios at medium to large shear strain levels – as indicated by the comparison between Masing rule result and the rest results. SANISAND-MSu model agrees better with Darendeli's empirical results, which gives confidence in using SANISAND-MSu model in earthquake analyses. Besides, SANISAND-MSu predicts a reduction of the damping ratio at relatively high strain

levels – larger than typically 0.5% in this case. Undrained sand exhibits such performance after entering the cyclic mobility or soil dilative behavior at larger strain levels, as also observed in lab tests results [29].

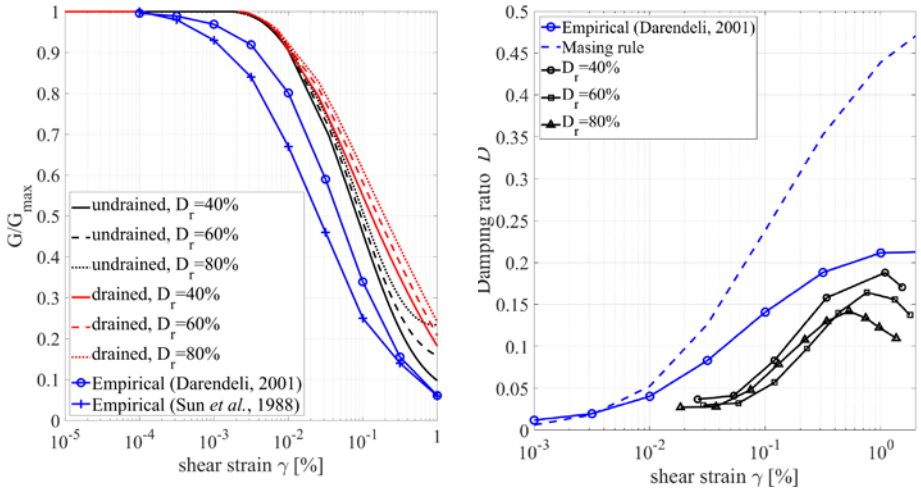

(a) Stiffness degradation (b) Damping ratio

Fig. 4. SANISAND-MSu model simulation results for (a) stiffness reduction and (b) damping ratio as function of shear strain. The simulations are performed under load controlled undrained cyclic DSS condition, with σ_{v0} =200 *kPa*.

3 Application of SANISAND-MSu in Offshore Energy Design

This section discusses representative results for the earthquake response of offshore energy structures founded on liquefaction-prone ground. Implicit 3D Finite Element modelling is performed using the open-source FE platform OpenSEES with the SANISAND-MSu as the user-defined material. Monopile response subject to quasi-static cyclic loading is first presented in Section 3.1 with focus on the effect of pore-water pressure. Section 3.2 is devoted to the dynamic response of two types of offshore energy-related structures, namely, wind turbines founded on monopiles and manifolds resting on mudmats. Karlsruhe fine sand, as described in Section 2, was selected for the simulation purposes with the model parameters listed in Table 1.

3.1 Monopile response under quasi-static cyclic loading

Effects of pore-water pressure on the cyclic response of monopile was studied using the 3D FE model presented in Fig. 5. The monopile has the following geometry features: pile embedded length L_{pile} =25 m, pile outer diameter D_{pile} =5 m (hence, aspect ratio L_{pile}/D_{pile}=5, which is comparable to a monopile supporting 5-MW offshore wind turbine) and pile wall thickness = 10 cm. The soil profile is assumed to have a uniform relative density D_r =80%

The monopile is assumed to be subject to symmetrical sinusoidal load cycles that are applied at the pile head (soil surface level), which means the load eccentricity is zero. Such a loading does not represent a realistic condition for monopiles of wind turbines. However, the objective is to better understand the response of large monopiles when their cyclic motions generate pore pressure in the soil.

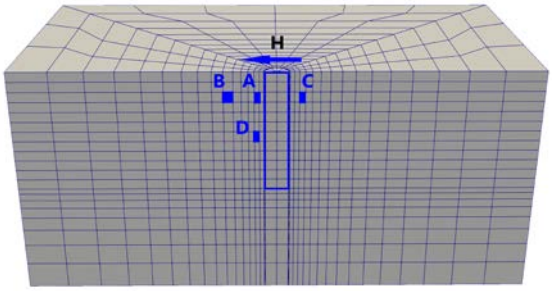

Fig. 5. FE model domain for quasi-static analysis.

To highlight the effects of pore-water pressure, two different simulations are performed: (1) monopile cyclic response under fully drained condition – which is realized by setting large permeability: 10^{10} *m/s*; (2) monopile cyclic response under fully undrained condition, in which case the permeability is set to 10^{-10} *m/s*. The number of loading cycles is limited to 10 which is a realistic representation of moderate to strong earthquake loading [31]. Detailed FE model settings can be found in [24].

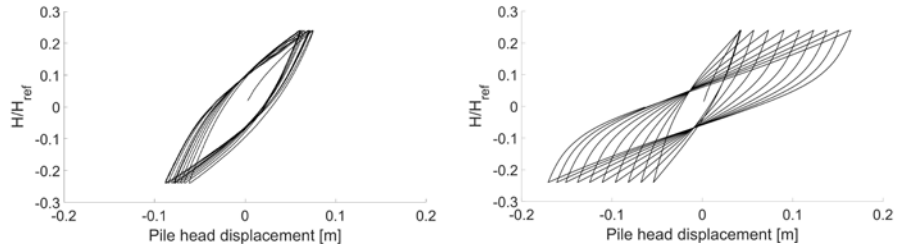

(a) Drained (b) Undrained

Fig. 6. Simulated pile force-displacement response for: (a) drained and (b) undrained sand.

Fig. 6 compares the pile head load-displacement results obtained for the two drainage conditions. The normalized load ratio H/H_{ref} is selected to represent the load level, with H_{ref} being the horizontal load applied at the pile head to induce a displacement $0.1D_{pile}$ at the pile head for drained condition. Fig. 6a shows that for the first loading cycle, $N = 1$, a non-closed load-displacement loop is formed due to the soil inhomogeneity induced by the initial virgin loading (when the initial loading up to H reaches its maximum value for the first time). Pile head displacement decreases from 0.07 m after the initial virgin loading to about 0.05 m after the first re-loading at $H = H_{max}$

(i.e., $N = 2$). For the following loading cycles, the pile head displacement at $H = H_{max}$ keeps increasing slowly. For the undrained simulation (Fig. 6b), rapid increase of pile displacement or progressive softening pile response, is induced with loading cycles.

The distinct behaviour captured in the two simulations can be attributed to different mechanisms, including:

(1) the generation and accumulation of the pore-water pressure in undrained case progressively reduces soil stiffness and thus leads to larger strain in the surrounding soils at large N. The surrounding soil in general shows stiffer behaviour in drained simulation.

(2) soil fabric evolves differently under the two drainage conditions. Under undrained condition, the rapid reduction of the mean effective stress accelerates the soil entering the dilative phase before the load increment reversal. Upon repeated unloading and reloading, the state of soil element likely alters from dilative to contractive to dilative. Such a process largely erases the load-induced fabric. In other words, sand fabric stiffening effects in the undrained simulation is smaller than that in drained simulation in the scope of current simulation.

Fig. 7 presents the soil resistance against pile displacement response (that is, cyclic $p - y$ response) simulated using SANISAND-MSu enhanced implicit 3D FE. Two different representative depths say $z = 2.5D_{pile}$ and $0.3D_{pile}$, are studied.

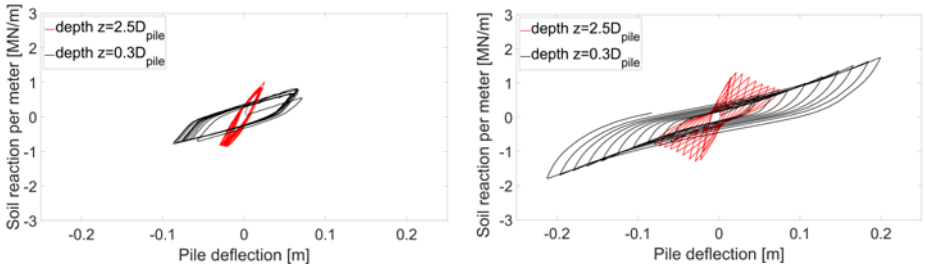

(a) Drained (b) Undrained

Fig. 7. Soil resistance against pile displacement: comparison between (a) drained and (b) undrained simulation results using SANISAND-MSu model.

For the drained simulation, (Fig. 7a), stable cyclic $p - y$ loops are obtained after the second loading cycle for both depths. For the undrained case, shown in Fig. 7b, the soil reaction first increases then decease at deep soil layer ($z = 2.5D_{pile}$). However, at shallow depth ($z = 0.3D_{pile}$), the soil reaction keeps increasing with loading cycles, which might be the direct result of easy soil dilatancy being triggering under undrained condition when initial stress level is low.

Fig. 8 presents the stress paths ($q \sim p$ response, Fig. 8a and Fig. 8c) and stress-strain responses ($\tau \sim \gamma$ response, Fig. 8b and Fig. 8d) for the two selected soil elements A and C as indicated in Fig. 5. Different colors represent for the lode angle defined within $0° \sim 60°$ as indicated by the color bar. Soil element A lies on the fore side (the left-hand side of the monopile in Fig. 5 of the monopile. It enters cyclic mobility regime after only one loading cycle, as shown in Fig. 8a, with shear strain γ, presented in see Fig.

8b, evolving mostly at moments lode angle equals to 0° (corresponding to triaxial compression) or 60° (triaxial extension). For element C that lies on the rear side (i.e., the right-hand side of the pile in Fig. 5) of the pile, more loading cycles are required to trigger the initial liquefaction (Fig. 8c), despite of the same initial mean effective stress. The accumulated strain is much smaller in element C compared with that in element A. Besides, the lode angle that corresponds to the rapid γ evolution (Fig. 8d) differs from that as indicated in Fig. 8b.

Understanding the local soil behaviour and pore-pressure generation are believed to be the key in the estimation of pile tilting due to cyclic loading and during earthquake shaking combined with environmental loading.

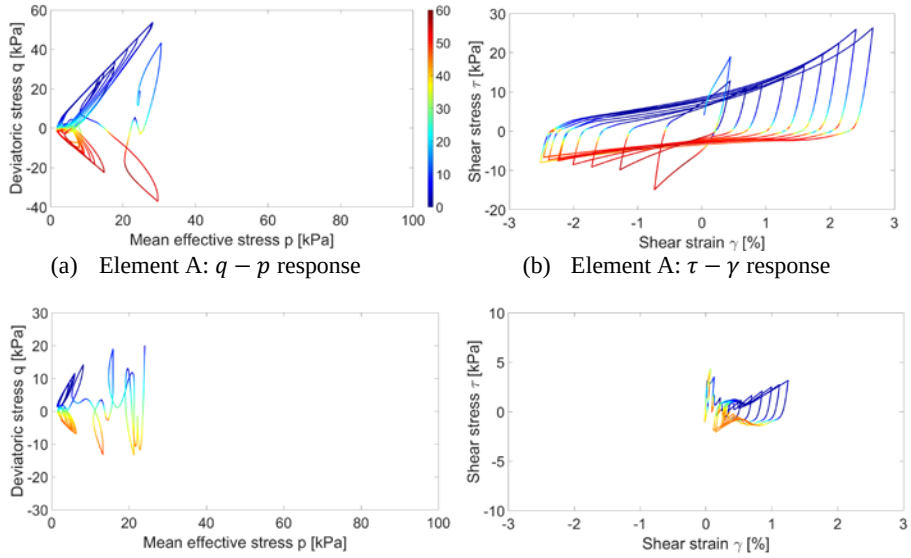

(a) Element A: $q - p$ response (b) Element A: $\tau - \gamma$ response

(c) Element C: $q - p$ response (d) Element C: $\tau - \gamma$ response

Fig. 8. Local soil response at selected elements: (a)-(b) Element A and (c)-(d) Element C (for element locations, see **Fig. 5**).

3.2 Dynamic response of offshore structures

In this section, the earthquake responses of structures founded on mudmat and monopiles in liquefiable soil are investigated through 3D nonlinear SANISAND-MSu enhanced dynamic analyses. In total, four simulation cases are included: two for a mudmat foundation for a subsea manifold and two for a monopile foundation used for an offshore wind turbine. The recorded earthquake, Kobe-L [14, 31], was used for the simulation purpose as indicated in Fig. 9. Uniform sand profile with relative density $D_r = 50\%$ and permeability $k_{soil} = 10^{-5}$ m/s was used in the analyses in this section. The earthquake shaking was applied to the base of the models. The tied boundary condition was employed to link the two side boundaries as successfully employed in [14]. The

earthquake response is studied through pore-water pressure evolution as well as the foundation motions.

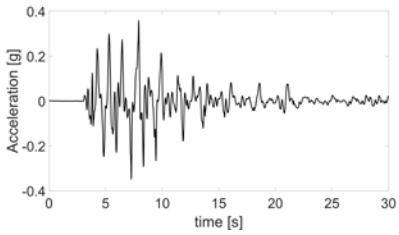

Fig. 9. Acceleration time history for horizontal component of Kobe-L earthquake.

Dynamic response of wind turbine on XL monopile.

The so-called 'XL monopile' (monopiles with diameter exceeding 7 m) has become a practical offshore foundation solution in response to the demand for economic construction of larger and more efficient wind turbines. In the present study, a 3D FE model with monopile diameter equal to 9 m was constructed as illustrated in Fig. 10.

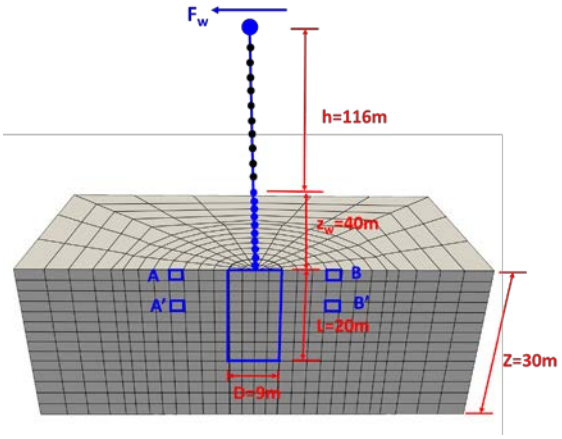

Fig. 10. FE model domain with wind turbine on XL monopile

A monopile with an embedded length $L = 20$ m, which corresponds to an aspect ratio $\frac{L}{D_{pile}} = 2.22$, has been adopted for the analyses. This aspect ratio is currently considered the limit for plausible monopile foundations. The other parameters of the structure are the wall thickness t_{pile} of monopile =10 cm (giving $\frac{t_{pile}}{D_{pile}} = 0.011$), pile length above soil surface (transition piece) =40 m (in sea water), the tower length = 116 m, and mass density of tower material = 7850 kg/m^3. In addition, a lumped mass of 700,000 kg is placed at the top of the tower to represent the masses of rotor and nacelle and a mass of 500,000 kg was distributed in 23 m above the sea level to represent the mass of the

transition piece and added hydrodynamic mass. A Rayleigh damping ratio of 2% was adopted at the frequencies 0.35 Hz and 1.75 Hz. A relatively coarse mesh was used for the soil domain without performing mesh sensitivity checks. The same mesh size was shown to be satisfactory for high-level assessments of the response in [14]. For simulations involving wind load, a static lateral load of 700 kN is applied at the hub.

The distributions of the pore-water pressure ratios at the end of the earthquake shaking ($t = 30$ s) are summarized in Fig. 11. The SANISAND-MSu simulation result (Fig. 11 b) is compared with that using SANISAND04 model (Fig. 11a) to highlight the influence of the adopted constitutive model on the pore-water pressure evolution in the soil domain during . The loading condition is the combined earthquake shaking (horizontal motion applied at the soil base) and a constant wind load applied at the hub as indicated in Fig. 10.

Both simulations clearly demonstrate soil liquefaction on the fore side of the monopile (the left hand-side of the monopile as indicated in Fig. 10) with the SANISAND04 simulation indicating a significantly larger liquified soil zone. None of the simulations indicate any noteworthy pore-water pressures inside the monopiles, as also observed and discussed in [14]. On the rear side of the monopile (i.e., right-hand side of the model), only a limited liquefaction zone is observed away from the monopile in SANISAND-MSu simulation case. However, SANISAND04 simulation results suggests no significant difference between the two sides which could be because free-field liquefaction is more prevalent when using SaniSAND04. Negative pore-water pressure ratios (r_u) are detected in shallow soil layers and below soil tip on the fore side of the monopile in both simulation cases. For SANISAND-MSu simulation, negative r_u is also detected on the rear side of the monopile in the shallow layers.

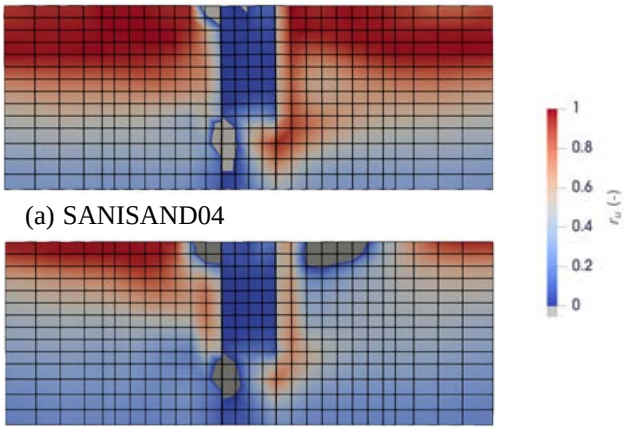

(a) SANISAND04

(b) SANISAND-MSu

Fig. 11. Distribution of pore-water pressure ratio. Simulations using (a) SANISAND04 and (b) SANISAND-MSu. Loading case: combined earthquake shaking and wind load.

Fig. 12 presents the time-history of the pore-water pressure ratio at selected elements A' and B' (ref. Fig. 10). For both elements, SANISAND-MSu simulations indicate

smaller peak r_u values compared with SANISAND04. The different pore-water distribution in Fig. 11 and the time evolutions in Fig. 12 are the direct consequences of the different hardening laws in the two models. As explained earlier, SANISAND-MSu model accounts for the load-induced sand fabric stiffening in the pre-dilative soil response and thus delays the occurrence of initial liquefaction.

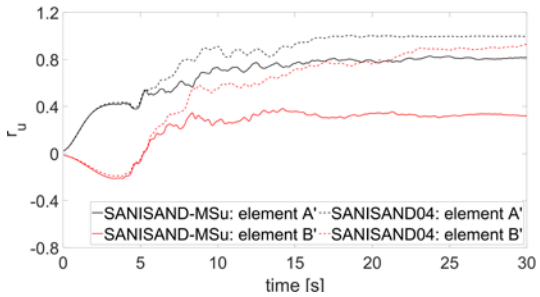

Fig. 12. Time history of pore-water pressure ratio at selected elements A' and B' (ref. Fig. 10) using both SANISAND04 and SANISAND-MSu for combined earthquake and wind load.

Fig. 13 summarizes the SANISAND-MSu simulation results of r_u evolutions at the four representative soil elements (indicated in Fig. 10), under combined earthquake shaking and wind load. On the fore side of the monopile (element A and A'), relatively large r_u values are obtained for both shallow soil (element A) and deeper soil (element A'). An opposite conclusion is drawn on the rear side of the monopile: initial liquefaction is triggered in neither element with the element at shallower layer showing smaller r_u compared with the element at deeper layer.

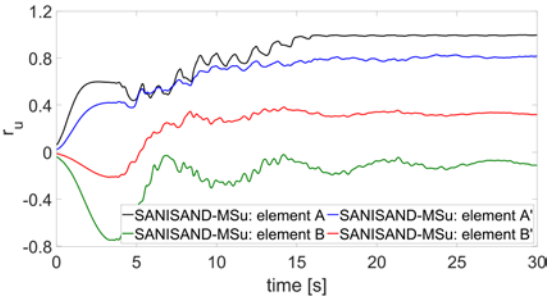

Fig. 13. Time history of pore-water pressure ratio at selected elements A, B, A' and B' in Fig. 10 using SANISAND-MSu for combined earthquake shaking and wind load.

As mentioned above, the accumulation of pore-water pressure alters the soil stiffness and affects the foundation behavior. This conclusion can be confirmed by the plots in Fig. 14, which display the time histories of the hub horizontal displacement (Fig. 14a) and the pile head rotation (Fig. 14b). As expected, SANISAND04 simulation generates larger hub displacement U_x and larger pile head rotation θ_r. The observed differences in rotations can be explained by the same principles described in Section 2.1.

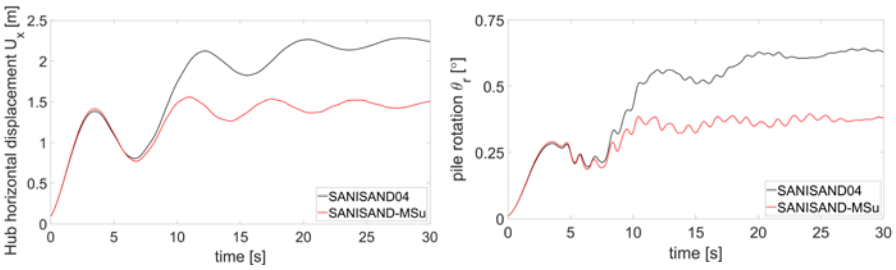

(a) Hub horizontal displacement (b) Pile head rotation

Fig. 14. Comparison of time histories of (a) hub horizontal displacement and (b) pile head rotation using SANISAND04 and SANISAND-MSu models for combined earthquake and wind load.

These results have important design implications. Following the pile rotation limit specified in DNV-OS-J101 [30] for the normal drivetrain operation, SANISAND-MSu predicts rotations within the acceptable limit while SANISAND04 indicates unacceptable performance.

For reference, the distribution of r_u under only earthquake shaking is presented in Fig. 15. Pore-water pressure ratio is nearly symmetrical on both sides of the monopile. No negative r_u is detected which is different from the case with wind load and tower inertia as observed in Fig. 11b. Therefore, the simultaneous loading from earthquake and wind lead to a more critical condition regarding liquefaction.

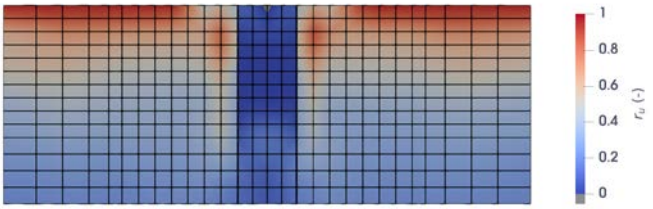

Fig. 15. Distribution of pore-water pressure ratio for earthquake shaking only.

The effect of wind load on the vertical displacement and rotation of the monopile are presented in Fig. 16. When subjected to solely earthquake shaking, the accumulated vertical displacement (Fig. 16a) after the shaking is nearly zero; this is significantly smaller than the displacement in the presence of the wind load (9.5 cm in this case). However, for the two loading conditions, the amplification of the vertical displacement during shaking are comparable. Similar conclusion can be drawn from the pile rotation response under the two loading conditions as indicated in Fig. 16b; namely, there is nearly no permeant pile head rotation accumulated after the shaking for pure earthquake loading, while for combined wind load and earthquake shaking the permanent tilt of the monopile reaches nearly 0.4° which is very close to the normal operational limit set by DNV-OS-J101 (0.5°) [32].

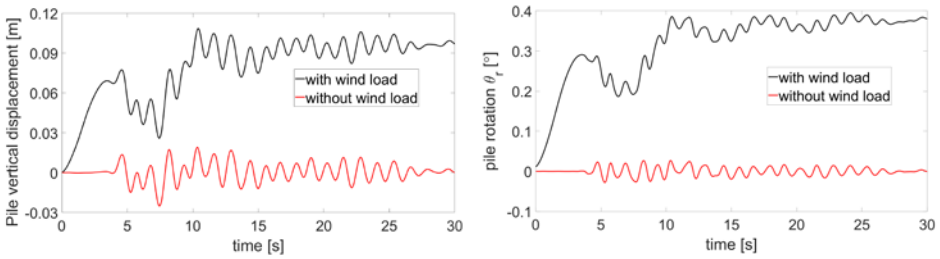

(a) Pile vertical displacement (b) Pile head rotation

Fig. 16. Pile response subject to earthquake shaking with and without wind load: (a) vertical displacement and (b) rotation.

Dynamic response of manifold on mudmat.

Fig. 17 illustrates the three-dimensional models used for the simulation of the response of a manifold on a mudmat. The mudmat has a dimension (width × length ×height) = 15m × 15m × 5m; however, due to symmetry of the simulated case, only half of the width, that is, 7.5m, is modelled), the same as that adopted in [20]. The dimensions of the soil domain are indicated in the figure.

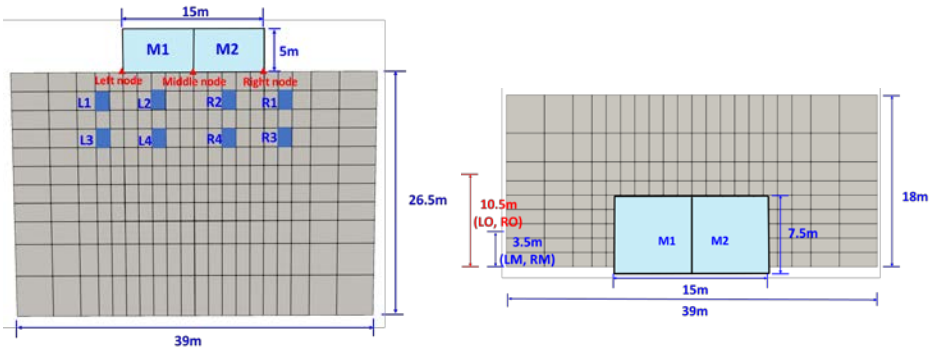

(a) Front view (b) Top view

Fig. 17. FE model domain: mudmat simulation.

An earlier study by Esfeh et al. [20] has indicated generally small rotations for typical symmetrical manifolds during earthquake shaking and in presence of liquefaction. The objective of the analyses in this section is to study the effect of manifold's unsymmetrical configuration in a simple model. To this end, two simulations were performed: a) mudmat with symmetric manifold, and b) mudmat with unsymmetrical mass distribution of manifold (denoted as symmetric case and unsymmetrical case in the following). For the symmetric case, the masses for parts $M1$ and $M2$ (See Fig. 17) are both 60, 000 kg (and therefore a total mass of 120,000 kg). For the unsymmetrical case, $M1$ has a

mass of 80,000 kg, while $M2$ has a mass of 40,000 kg (same total weight as the symmetric case). The same Rayleigh damping parameters were used in this model.

The distribution of the pore-water pressure ratio at times $t = 20$ s and 30 s are presented in Fig. 18. In general, simulations of both symmetric and unsymmetrical cases indicate that liquefaction can be triggered at shallow soil layers, with pore-water pressure ratios in the elements beneath the mudmat tending to be smaller than those in the outer elements.

At $t = 20\ s$, different r_u distributions are achieved for the two simulations. For the symmetric case, r_u distribute almost symmetrically. While for the unsymmetrical simulation case, large pore-water pressure ratio (larger than 0.8) is triggered in elements not only at shallow soil layer, but also in the area located slightly deeper and outside $M2$ (the part with smaller mass). A possible reason can be the different initial mean effective stresses at different zones if the manifold mass is distributed unsymmetrically. More specifically, on the side with smaller mass, the initial mean effective stress is smaller than the other side; therefore, the soil elements on the lighter side tend to accumulate more pore-water pressure under the same shaking and inertial load of the manifold. At $t = 30$ s, the differences in r_u distribution for two simulation cases become negligible.

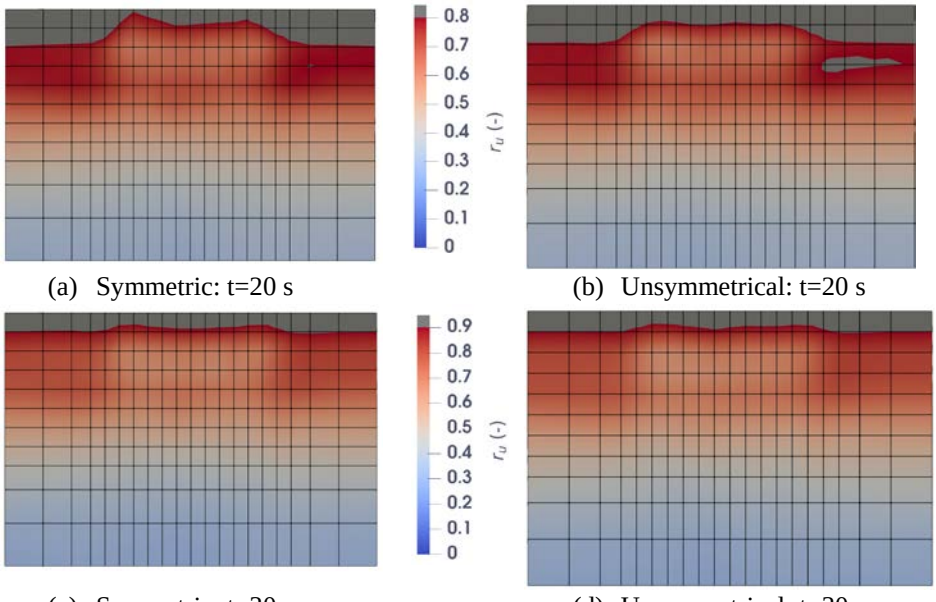

(a) Symmetric: t=20 s (b) Unsymmetrical: t=20 s

(c) Symmetric: t=30 s (d) Unsymmetrical: t=30 s

Fig. 18. Distribution of pore-water pressure ratios at time t= 20 s and t = 30 s. for symmetric and unsymmetrical cases (refer to figure texts for cases).

It is also instructive to compare the time histories of r_u for both the symmetric case (Fig. 19a) and the unsymmetrical case (Fig. 19b) at different representative elements $L1{\sim}L4$ and $R1{\sim}R4$ as indicated in Fig. 17a.

For the symmetric case (Fig. 19a), elements lying at shallow soil layer ($L1, L2, R1$ and $R2$) enter the liquefaction state at the end of the shaking. However, elements that lie outside the mudmat edge (elements L_1 and R_1) enter liquefaction much earlier than the elements within the mudmat edge (elements L_2 and R_2). For elements at deeper soil layer ($L3, L4, R3$ and $R4$), liquefaction is triggered.

For unsymmetrical case (Fig. 19b), soil elements at relatively deeper depth ($L3, L4, R3$ and $R4$) show almost same trend as in the symmetric case. At shallow layer, element $R1$ shows difference in r_u evolution when compared with $L1$ response – the element located outside $M1$ edge, that is, element $L1$ enter liquefaction earlier than the element located outside $M2$ edge (element $R1$).

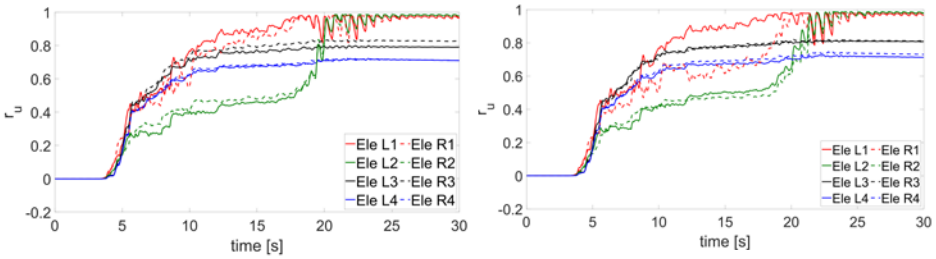

(a) Symmetric (b) Unsymmetric

Fig. 19. Evolution of pore-water pressure ratio at representative soil elements (see Fig. 17), simulation cases of: (a) symmetric manifold, and (b) unsymmetrical manifold.

Finally, Fig. 20 compares the responses of the mudmats for the symmetric and unsymmetrical cases. As expected, for the horizontal displacement (Fig. 20a), no significant differences are observed for the two simulation cases. For the rotation, on the other hand (Fig. 20b), the unsymmetrical case experiences considerably larger mudmat rotation compared with the symmetric case. This is an important consideration in design of heavy subsea facilities if a simple (so-called stick) model of the manifold is adopted for the global response of the system. These results indicate that one should properly capture the unsymmetrical stress distribution under the mudmat in the analyses.

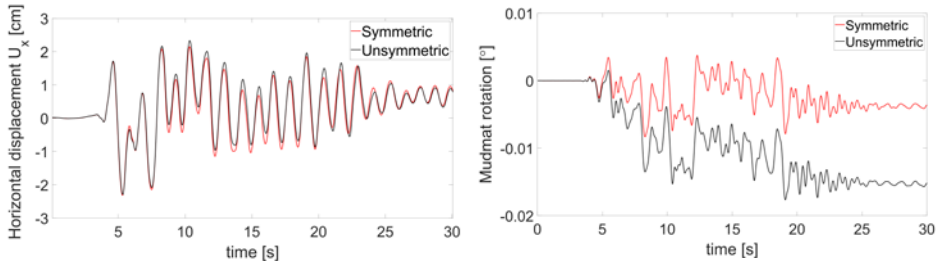

(a) Horizontal displacement (b) rotation

Fig. 20. Time history of horizontal displacement and rotation of mudmat during the Kobe-L earthquake shaking for symmetric and unsymmetrical manifolds.

4 Conclusion

The features and performance of SANISAND-MSu model in reproducing the soil element response has been presented in this paper. The model is shown to be reasonable in reflecting the soil undrained cyclic behavior, in particular, in terms of cycle-by-cycle pore water pressure accumulation and progressive strain accumulation in the cyclic mobility regime. Subsequently, SANISAND-MSu model is implemented into OpenSEEs for analysis of two types of offshore energy structure.

Pore-water pressure effects on monopile lateral behaviour is first studied under quasi-static cyclic loading. The simulation results indicate progressive decreasing of pile stiffness due to increasing of the pore-water pressure in the surrounding soil. The simulated cyclic $p-y$ response is also presented. Local soil elements responses are extracted. The $q{\sim}p{\sim}\theta$ (mean effective stress ~ deviatoric stress ~ Lode angle) and $\tau{\sim}\gamma{\sim}\theta$ (shear stress ~ shear strain ~ Lode angle) relationships of the selected elements suggests that for soil elements located at the symmetry plane, shear strain is mostly generated when the mean effective stress is small and the Lode angle enters 'triaxial compression' and 'triaxial extension' states.

Dynamic response of an XL monopile (pile diameter of 9 m with aspect ratio $\frac{L_{pile}}{D_{pile}} = 2.22$) has been studied. The horizontal component of Kobe-L earthquake shaking is applied at the base of the soil. The simulation results indicate that soil liquefaction mainly occur at shallow soil layers and outside of the monopile. For soils inside the monopile, negligible increase in pore-water pressure can be observed. For the loading case with only earthquake shaking, very small accumulated pile displacement (or pile head rotation) is achieved. While if the earthquake shaking is combined with the static load wind applied at turbine hub (which is the most probable load case in reality), the loading can significantly increase the pile head rotation. Besides, in the combined wind load and earthquake shaking, the soil elements located in the fore side of the monopile are more likely to liquefy.

Effect of mass distribution on the dynamic response of a manifold over a mudmat is also studied. Soil elements beneath the mudmat but inside the foundation edge can might need longer shaking to enter liquefaction. For the unsymmetrical mass distribution, during earthquake shaking, soil elements located beneath the lighter side and outside the mudmat edge show slightly higher pore-water pressure ratios. However, such a difference progressively vanishes after the strong shaking. With the same total weight, the unsymmetrical weight distribution leads to a larger foundation rotation compared with the case where the weight is distributed symmetrically.

The simulations in this work aim to give general impression on the cyclic and dynamic response of two typical offshore structures using SANISAND-MSu enhanced 3D FE analysis approach. Detailed calibration of model parameters and more rigorous consideration of the model dynamic properties need to be undertaken together with more refined FE mesh, are required to achieve more accurate results in actual design cases. Regardless, sensitivity analyses are highly encouraged considering the uncertainties in the soil parameters and the computational models.

References

1. Europe Wind. Offshore wind in Europe: Key trends and statistics 2019 (2020).
2. IEA, Offshore wind outlook 2019. Tech. rep. (2019).
3. Bransby, M., Randolph, M.: Combined loading of skirted foundations. Géotechnique 48(5), 637–655 (1998).
4. Byrne, B.W., Houlsby, G.T.: Experimental investigations of the response of suction caissons to transient combined loading. Journal of geotechnical and geoenvironmental engineering 130(3), 240–253 (2004).
5. Byrne, B., Houlsby, G.: Assessing novel foundation options for offshore wind turbines. In: World maritime technology conference. London, (2006).
6. LeBlanc, C., Houlsby, G.T., Byrne, B.W.: Response of stiff piles in sand to long-term cyclic lateral loading. Géotechnique 60(2), 79–90 (2010).
7. Wang, X., Yang, X., Zeng, X.: Seismic centrifuge modelling of suction bucket foundation for offshore wind turbine. Renewable energy 114, 1013–1022 (2017).
8. Richards, I., Bransby, M., Byrne, B., Gaudin, C., Houlsby, G.: Effect of stress level on response of model monopile to cyclic lateral loading in sand. Journal of Geotechnical and Geoenvironmental Engineering 147(3), 04021002 (2021).
9. Cuéllar, P., Mira, P., Pastor, M., Merodo, J.A.F., Baeßler, M., Rücker, W.: A numerical model for the transient analysis of offshore foundations under cyclic loading. Computers and Geotechnics 59, 75–86 (2014).
10. Tasiopoulou, P., Chaloulos, Y., Gerolymos, N., Giannakou, A., Chacko, J.: Cyclic lateral response of OWT bucket foundations in sand: 3D coupled effective stress analysis with Ta-Ger model. Soils and Foundations 61(2), 371–385 (2021).
11. Liu, H.Y., Kementzetzidis, E., Abell, J.A., Pisanò, F.: From cyclic sand ratcheting to tilt accumulation of offshore monopiles: 3D FE modelling using SANISAND-MS. Géotechnique pp. 1–16 (2021).
12. Chaloulos, Y.K., Tsiapas, Y.Z., Bouckovalas, G.D.: Seismic analysis of a model tension leg supported wind turbine under seabed liquefaction. Ocean Engineering238, 109706 (2021).
13. Kaynia, A.M.: Seismic considerations in design of offshore wind turbines. Soil Dynamics and Earthquake Engineering 124, 399–407 (2019).
14. Esfeh, P.K., Kaynia, A.M.: Earthquake response of monopiles and caissons for offshore wind turbines founded in liquefiable soil. Soil Dynamics and Earthquake Engineering 136, 106213 (2020).
15. Jostad, H.P., Dahl, B.M., Page, A., Sivasithamparam, N., Sturm, H.: Evaluation of soil models for improved design of offshore wind turbine foundations in dense sand. Géotechnique 70(8), 682–699 (2020).
16. Corciulo, S., Zanoli, O., Pisanò, F.: Transient response of offshore wind turbines on monopiles in sand: role of cyclic hydro–mechanical soil be-haviour. Computers and geotechnics 83, 221–238 (2017).
17. Yang, Z., Elgamal, A.: Multi-surface cyclic plasticity sand model with lode angle effect. Geotechnical and Geological Engineering 26(3), 335–348 (2008).
18. Kementzetzidis, E., Corciulo, S., Versteijlen, W.G., Pisano, F.: Geotechnical aspects of offshore wind turbine dynamics from 3D non-linear soil-structure simulations. Soil Dynamics and Earthquake Engineering 120, 181–199 (2019).
19. Dafalias, Y.F., Manzari, M.T.: Simple plasticity sand model accounting for fabric change effects. Journal of Engineering mechanics 130(6), 622–634 (2004).
20. Esfeh, P.K., Govoni, L., Kaynia, A.M.: Seismic response of subsea structures on caissons and mudmats due to liquefaction. Marine Structures 78, 102972 (2021).

21. Liu, H.Y., Abell, J.A., Diambra, A., Pisanò, F.: Modelling the cyclic ratcheting of sands through memory-enhanced bounding surface plasticity. Géotechnique 69(9), 783–800 (2019).
22. Corti, R., Diambra, A., Muir Wood, D., Escribano, D.E., Nash, D.F.: Memory surface hardening model for granular soils under repeated loading conditions. Journal of Engineering Mechanics p. 04016102 (2016).
23. Liu, H.Y., Diambra, A., Abell, J.A., Pisanò, F.: Memory-enhanced plasticity modeling of sand behavior under undrained cyclic loading. Journal of Geotechnical and Geoenvironmental Engineering 146(11), 04020122 (2020).
24. Liu, H.Y., Kaynia, A.M.: Characteristics of cyclic undrained model SANISAND-MSu and their effects on response of monopiles for offshore wind structures. Géotechnique pp. 1–39 (2021).
25. Been, K., Jefferies, M.G.: A state parameter for sands. Géotechnique 35(2), 99–112 (1985).
26. Wichtmann, T., Triantafyllidis, T.: An experimental database for the development, calibration and verification of constitutive models for sand with focus to cyclic loading: part I — tests with monotonic loading and stress cycles. Acta Geotechnica 11(4), 739–761 (2016).
27. Sun, J.I., Golesorkhi, R., Seed, H.B.: Dynamic moduli and damping ratios for cohesive soils. Earthquake Engineering Research Center, University of California Berkeley (1988).
28. Darendeli, M.B.: Development of a new family of normalized modulus reduction and material damping curves. The university of Texas at Austin (2001).
29. Blaker, Ø., Andersen, K.H.: Cyclic properties of dense to very dense silica sand. Soils and Foundations 59(4), 982–1000 (2019).
30. Ramirez, J., Barrero, A.R., Chen, L., Dashti, S., Ghofrani, A., Taiebat,M., Arduino, P.: Site response in a layered liquefiable deposit: evaluation of different numerical tools and methodologies with centrifuge experimen-tal results. Journal of Geotechnical and Geoenvironmental Engineering144(10), 04018073 (2018).
31. Kramer, S.L.: Geotechnical earthquake engineering. Prentice-Hall Civil Engineering and Engineering Mechanics Series (1996).
32. DNV: Design of offshore wind turbine structures vol DNV-OS-J101. Det Norske Veritas, Høvik, Norway.